The Astrophysical Journal, 574:440–452, 2002 July 20

INTERACTION OF EIT WAVES WITH CORONAL ACTIVE REGIONS

L. Ofman
Catholic University of America at NASA Goddard Space Flight Center, Code 682, Greenbelt, MD 20771;
Leon.Ofman@gsfc.nasa.gov

and

B. J. Thompson
NASA Goddard Space Flight Center, Code 682, Greenbelt, MD 20771
Received 2001 October 31; accepted 2002 March 28

ABSTRACT

Large-scale coronal waves associated with flares were first observed by the *Solar and Heliospheric Observatory* (*SOHO*) Extreme ultraviolet Imaging Telescope (EIT). We present the first three-dimensional MHD modeling of the interaction of the EIT waves with active regions and the possibility of destabilization of an active region by these waves. The active region is modeled by an initially force-free, bipolar magnetic configuration with gravitationally stratified density. We include finite thermal pressure and resistive dissipation in our model. The EIT wave is launched at the boundary of the region, as a short time velocity pulse that travels with the local fast magnetosonic speed toward the active region. We find that the EIT wave undergoes strong reflection and refraction, in agreement with observations, and induces transient currents in the active region. The resulting Lorentz force leads to the dynamic distortion of the magnetic field and to the generation of secondary waves. The resulting magnetic compression of the plasma induces flows, which are particularly strong in the current-carrying active region. We investigate the effect of the magnetic field configuration and find that the current-carrying active region is destabilized by the impact of the wave. Analysis of the three-dimensional interaction between EIT waves and active regions can serve as a diagnostic of the active region coronal magnetic structure and stability.

Subject headings: MHD — Sun: corona — Sun: magnetic fields — waves
On-line material: color figures, mpeg animations

1. INTRODUCTION

Fast wave pulsations in coronal active region loops associated with impulsive events (such as flares) can be observed and used to determine the physical parameters of the plasma and field strength (Roberts, Edwin, & Benz 1983, 1984; Nakariakov et al. 1999; Nakariakov & Ofman 2001). Large-scale coronal waves were first observed by the *Solar and Heliospheric Observatory* (*SOHO*) Extreme ultraviolet Imaging Telescope (EIT) (Thompson et al. 1999, 2000) and hence were termed "EIT waves." The waves are associated with flares and coronal mass ejections (CMEs) and propagate at typical speeds of 200–500 km s^{-1}. Recently, it has been found using magnetic data from the Michelson Doppler Imager (MDI) with density information supplied by the EIT that in quiet regions of the low corona, a typical fast mode speed is about 200 km s^{-1}, while in active regions, the fast mode speed reaches several thousand km s^{-1} (Norton 2001). EIT waves were interpreted as fast magnetosonic waves (Wang 2000; Murawski, Nakariakov, & Pelinovsky 2001; Warmuth et al. 2001) and associated with Moreton waves observed in the photosphere (Moreton 1961).

Observations of impulsive phenomena at separate locations on the solar disk and occurring closely in time, which could be related through a propagating disturbance, are some of the earliest evidence of EIT waves and other large-scale coronal transients. The phenomenon of "sympathetic flaring" (Richardson 1951; Becker 1958; Valníček 1964; Wang et al. 2001) has recently been revisited by Biesecker & Thompson (2000), who demonstrated that there is no appreciable increase in the frequency of solar flares following the propagation of an EIT wave. The sympathetic flaring study was prompted by the observation of the EIT waves' long duration and far propagation and by observations that the EIT wave produces visible deflections in the ambient corona as it propagates (Thompson et al. 1999; Wills-Davey & Thompson 1999). However, the Biesecker & Thompson (2000) study is limited by the small number of on-disk waves analyzed (31) and the relatively low cadence of the EIT images (7–15 minutes per image).

There is additional evidence of long-range effects of EIT wave propagation. Some of the EIT observations indicate lingering evolution at filament channels as a result of wave passage; although the EIT cadence is too poor to isolate any periodicity, the phenomenon appears to be similar to the oscillating filaments reported by Ramsey & Smith (1966) and Smith & Harvey (1971) associated with flare waves. Krucker et al. (1999) established that impulsive electron events observed in association with solar flares at the east appear to correlated with westward-propagating EIT waves. Additionally, Klassen et al. (1999) demonstrate a high correlation (90%) between metric type II radio burst and EIT wave observations. As in the Pinter & Dryer (1977) study involving Moreton waves, the inferred speeds of the type II bursts did not match those of the associated EIT waves.

The first three-dimensional numerical simulation of the large-scale properties of EIT waves were performed recently by Wu et al. (2001). They investigated the global large-amplitude waves propagating across the solar disk, and they were able to identify the EIT waves as the fast magnetosonic mode and to compare favorably the morphology of the

simulated waves with EIT observations. Collision between shock waves and magnetic flux tubes in the photosphere was recently studied by Sakai et al. (2000) using three-dimensional MHD-neutral gas equations. They found that surface and body Alfvén waves together with strong plasma jets are excited in the flux tubes.

We present the first three-dimensional MHD simulation of the interaction between EIT waves and bipolar active regions in the corona. We find that the EIT waves undergo strong reflection and refraction, and excite secondary waves and flows in the bipolar active region with gravitationally stratified density. The flows are particularly strong in the current-carrying active region, which leads to instability. While present observations of the corona are limited to two-dimensional projections in the plane of the sky (with future three-dimensional capability in the planned *Solar Terrestrial Relations Observatory* [*STEREO*] mission), the modeling allows the investigation of the three-dimensional structure of the EIT wave interaction with active regions. The modeling combined with observations can serve as a diagnostic of active region structure and stability.

2. OBSERVATIONS

One of the major limitations of the EIT wave observations is the image cadence: consecutive images are separated by at least 9 minutes, making it difficult to observe rapidly evolving and propagating phenomena. Because a 500 km s^{-1} wave can travel from equator to pole in half an hour, few EIT wave observations consist of more than two or three images, and the evolution of local structures is nearly impossible to document in a quantitative sense. Nonetheless, a number of characteristics of wave morphology and propagation have been accumulated by comparing the vast number of events (>200) observed. The EUV telescope on board the *Transition Region and Coronal Explorer* (*TRACE*) provides high-resolution images and with better time cadence than *SOHO*/EIT (Handy et al. 1998). *TRACE* observations enabled direct high-cadence observation of active region distortion and coronal loop oscillations induced by EIT waves (Wills-Davey & Thompson 1999; Aschwanden et al. 1999; Nakariakov et al. 1999).

In the present study we are focused on the local interaction of the EIT wave with the active region, rather than with the global propagation characteristics of the wave on the solar disk (Wu et al. 2001). Several features of EIT wave propagation are most relevant to this paper: (1) EIT waves are observed to propagate primarily in the ambient corona and are deflected away from active regions; (2) the long-range propagation of EIT waves observed at the solar limb consists primarily of a deflection of magnetic features, similar to sheaves of wheat blowing in a field; (3) deflection of magnetic features at the edge of active regions along with the EIT wave passage is occasionally observed (image timing and cadences greatly influences the ability to observe this phenomenon); (4) in some events the "lingering" of evolution is observed when the wave reaches some solar features, such as a filament channel; and (5) EIT waves exhibit a fairly standard range in the observed velocity of large-scale propagation (190–500 km s^{-1}), apparently independent of the speed or magnitude of the impulse.

Although EIT waves are named for the instrument with which they are primarily observed, the *TRACE* mission and possibly the Soft X-ray Telescope (SXT) on board *Yohkoh* have captured the phenomenon in their imagery. Recent SXT observations by Khan & Hudson (2000) show a propagating disturbance emanating from a flaring active region from which develops an extremely fast (1760 km s^{-1}) CME. Because the emission observed by SXT is typically hotter than the EUV corona, it is assumed that the wave documented by Khan & Hudson (2000) represents an extremely energetic example of an EIT wave. *TRACE* observations by Wills-Davey & Thompson (1999) show a "typical" EIT wave concurrent with EIT observations of the same event. The overlapping observations combine the higher spatial (0.″5–1″ $pixel^{-1}$) and temporal (~1 minute) resolution and multiwavelength (171, 195, and 1216 Å) coverage of the *TRACE* instrument with the full-disk view provided by the EIT instrument (5.″2 $pixel^{-1}$, 9–20 minutes between images). Wills-Davey & Thompson (1999) discuss the development of the wave as observed in the EIT images and explicit characteristics of the propagation as seen in the high-resolution *TRACE* data.

Figure 1 (adapted from Fig. 2 in Wills-Davey & Thompson 1999) shows the location of the *TRACE* observations plotted on an EIT 195 Å difference image of the 1998 June 13 disturbance. The location of the *TRACE* images allows an excellent view of the transit of the wave disturbance as it propagates through the ambient corona north of the erupting region. Figure 2 is an adaptation of Figure 3 from Wills-Davey & Thompson (1999). The figure shows the location of the disturbance in the *TRACE* field of view (the box in Fig. 1) at six different observation times, along with lines of propagation as computed by a Huygens plotting algorithm (*dashed lines*, indicating the nearest point on adjacent wave fronts). The active region from which the wave originates is located to the south of the *TRACE* observations.

The location of the wave fronts in Figure 2 illustrate the significant variability in the speed and direction of wave

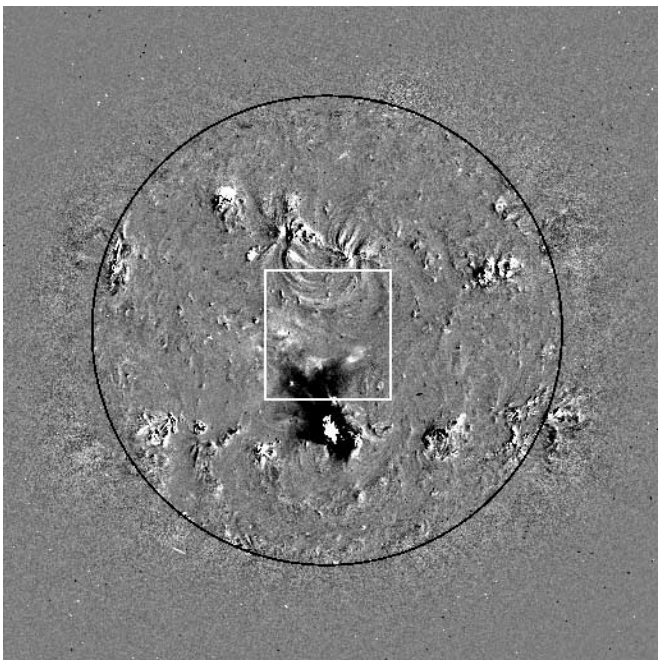

FIG. 1.—Location of the *TRACE* observations plotted on an EIT 195 Å difference image of the 1998 June 13 disturbance event (adapted from Wills-Davey & Thompson 1999).

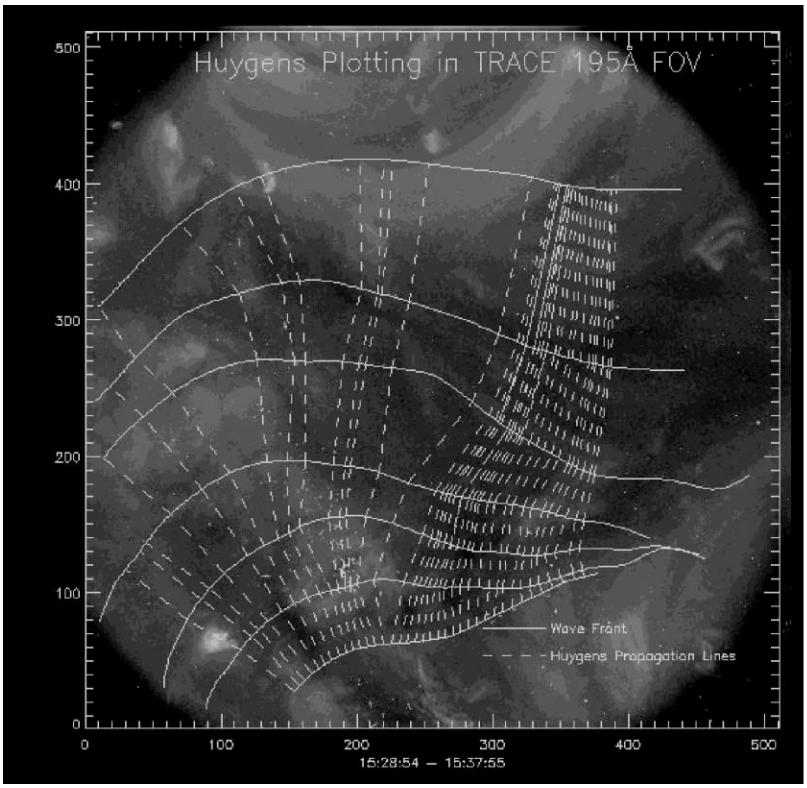

FIG. 2.—*TRACE* 195 Å image of the 1998 June 13 field of view that shows parts of an active region. The solid lines indicate the wave fronts of the propagating disturbance at seven successive times during 15:28:54–15:37:55 UT. The dashed lines show propagating trajectories of the disturbance (adapted from Wills-Davey & Thompson 1999).

propagation, The speeds range from 200 to 800 km s^{-1} in the *TRACE* field of view, exhibiting the highest velocity as the wave approaches the active region in the north. As implied by the EIT observations, the passage of the wave in the *TRACE* images is marked primarily by a local increase in emission caused by the deflection of magnetic field lines. Although the erupting region determines to a great extent the direction of propagation and the amplitude of the initial impulse, the propagation of the wave (particularly late in its transit when it is far from the region of its origin) depends heavily on the corona through which it is propagating. The propagating characteristics of the wave provide information on the local fast magnetosonic speed, allowing one to infer the structure of the corona through which the wave is propagating and ultimately to determine the three-dimensional structure of the coronal magnetic field.

3. THREE-DIMENSIONAL MHD MODEL

The MHD equations in flux conservative form with gravity and with standard notations for the variables are

$$\frac{\partial \rho}{\partial t} = -\nabla \cdot (\rho \boldsymbol{V}) \,, \tag{1}$$

$$\frac{\partial (\rho \boldsymbol{V})}{\partial t} = -\nabla \cdot \left[\rho \boldsymbol{V}\boldsymbol{V} - \boldsymbol{B}\boldsymbol{B} + \frac{1}{2}(B^2 + p)\boldsymbol{I}\right] - \frac{GM_\odot \rho}{r^2}\hat{\boldsymbol{r}} \,, \tag{2}$$

$$\frac{\partial \boldsymbol{B}}{\partial t} = \nabla \times \left[(\boldsymbol{V} \times \boldsymbol{B}) - \frac{1}{S}\nabla \times \boldsymbol{B}\right] \,, \tag{3}$$

$$\frac{\partial u}{\partial t} = -\nabla \cdot \left[(u + p)\boldsymbol{V} + (B^2 \boldsymbol{I} - 2\boldsymbol{B}\boldsymbol{B}) \cdot \boldsymbol{V} + \boldsymbol{S}_h\right] \,, \tag{4}$$

where $u = \frac{1}{2}\rho V^2 + B^2/8\pi + p/(\gamma - 1) - GM_\odot \rho / r$ is the energy density and $\boldsymbol{S}_h$ is the heating source. For Ohmic heating, $\boldsymbol{S}_h = (2/S)(\boldsymbol{B} \cdot \nabla \boldsymbol{B} - \nabla \boldsymbol{B} \cdot \boldsymbol{B})$ (e.g., Schnack & Killeen 1980). For $\gamma = 1$ used here, the energy equation (4) simplifies to the isothermal equation $p = T_0 \rho$. In the above equations S is the magnetic Reynolds number. Viscosity is neglected in the present model.

The initial bipolar, force-free magnetic field configuration of the model active region is given by (Cuperman, Ofman, & Semel 1989)

$$B_{x,j} = \frac{1}{r_j^2}\left[x_j \frac{r_j^2}{R_j^3}\cos(\alpha R_j) - \alpha \frac{x_j z_j^2}{R_j^2}\sin(\alpha R_j) + \alpha x_j \sin(\alpha z_j) + \alpha \frac{y_j z_j}{R_j}\cos(\alpha R_j) - \alpha y_j \cos(\alpha z_j)\right] \,, \tag{5}$$

$$B_{y,j} = \frac{1}{r_j^2}\left[y_j \frac{r_j^2}{R_j^3}\cos(\alpha R_j) - \alpha \frac{y_j z_j^2}{R_j^2}\sin(\alpha R_j) + \alpha y_j \sin(\alpha z_j) - \alpha \frac{x_j z_j}{R_j}\cos(\alpha R_j) + \alpha x_j \cos(\alpha z_j)\right] \,, \tag{6}$$

$$B_{z,j} = \frac{z_j}{R_j^3}\left[\cos(\alpha R_j) + \alpha R_j \sin(\alpha R_j)\right] \,, \tag{7}$$

where

$$R_j = r_j^2 + z_j^2 \ , \quad r_j^2 = x_j^2 + y_j^2 \ ,$$
$$x_j = x - x_{0,j} \ , \quad y_j = y - y_{0,j} \ , \quad z_j = z - z_{0,j} \ ,$$
$$x_1 = x - d \ , \quad x_2 = x - d \ ,$$
$$y_1 = y_2 = y \ , \quad z_1 = z_2 = z \ ,$$

with the resultant magnetic field components

$$B_{0,x} = B_{x,1} - B_{x,2} \ , \tag{8}$$
$$B_{0,y} = B_{y,1} - B_{y,2} \ , \tag{9}$$
$$B_{0,z} = B_{z,1} - B_{z,2} \ . \tag{10}$$

We have used potential ($\alpha = 0$) and current-carrying ($\alpha = 0.5$) field configurations in our numerical model.

The three-dimensional model active region is calculated in a computational box of the dimensions $(x_{\min}, x_{\max}) \times (y_{\min}, y_{\max}) \times (z_{\min}, z_{\max})$, where $-x_{\min} = x_{\max} = -y_{\min} = y_{\max} = 0.35\ R_\odot$, for the $\alpha = 0$ magnetic field and $0.42\ R_\odot$ for the $\alpha = 0.5$ case, with $z_{\min} = 0.1\ R_\odot$ and $z_{\max} = 0.4\ R_\odot$. In our coordinate system, the lower coronal boundary is at $z = z_{\min}$. At the lower coronal boundary, we impose the magnetic field given by equations (5)–(10) and use zero-order extrapolation for the velocity and the density, allowing flow through the boundary:

$$\boldsymbol{B}(x, y, z_{\min}, t) = \boldsymbol{B}_0(x, y, z_{\min}) \ ,$$
$$\boldsymbol{V}(x, y, z_{\min}, t) = \boldsymbol{V}(x, y, z_{\min} + \Delta z, t) \ ,$$
$$\rho(x, y, z_{\min}, t) = \rho(x, y, z_{\min} + \Delta z, t) \ , \tag{11}$$

where Δz is the grid separation in the z-direction. We use open boundary conditions at the other five boundary planes. At $x_{\min}$ and at $x_{\max}$ the boundary conditions are

$$\boldsymbol{B}(x_{\min,\max}, y, z) = \boldsymbol{B}(x_{\min,\max} \pm \Delta x, y, z) \ ,$$
$$\boldsymbol{V}(x_{\min,\max}, y, z) = \boldsymbol{V}(x_{\min,\max} \pm \Delta x, y, z) \ ,$$
$$\rho(x_{\min,\max}, y, z) = \rho(x_{\min,\max} \pm \Delta x, y, z) \ , \tag{12}$$

where Δx is the grid separation in the x-direction, the positive sign corresponds to $x_{\min}$, and the negative sign corresponds to $x_{\max}$. We use similar expressions for the boundary conditions at $y_{\min,\max}$ and at $z_{\max}$.

To model the impact of an EIT wave, we impose the following initial velocity pulse at $y = y_{\min}$:

$$V_y(x, y_{\min}, z, t) = A V_0(x, z) \ , \quad 0 < t < \delta t \ , \tag{13}$$

where the duration of the pulse is $\delta t = 10\tau_A$, where τ_A is the Alfvén time, V_0 is the local Alfvén speed, and A is the initial amplitude of the pulse. We have used $A = 0.25$ for the $\alpha = 0$ initial magnetic field (Fig. 3) and $A = 0.1$ for the $\alpha = 0.5$ initial magnetic field (Fig. 4). After a short transit time following the pulse, the boundary condition on V_y becomes open to allow flow through the boundary.

The gravitationally stratified initial number density is given by

$$n = n_0 e^{[1/(10+z-z_{\min})-0.1]/H} \ , \tag{14}$$

where H is the normalized scale height defined as $H = 2k_B T 0.1 R_\odot/(GM_\odot m_p)$ where k_B is Boltzmann's constant, T the temperature, G the gravitational constant, $M_\odot$

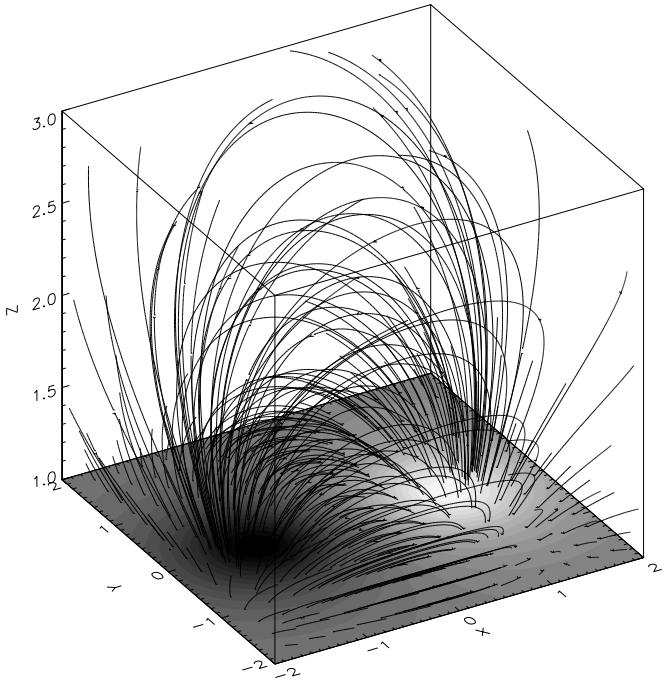

FIG. 3.—Three-dimensional structure of the potential initial magnetic field ($\alpha = 0$) of the model active region. The intensity plot at $z = 0$ of the B_z component shows the polarity of the field (dark is negative and bright is positive polarity). This figure is also available as an mpeg animation showing the impact of the wave in the electronic edition of the *Astrophysical Journal*.

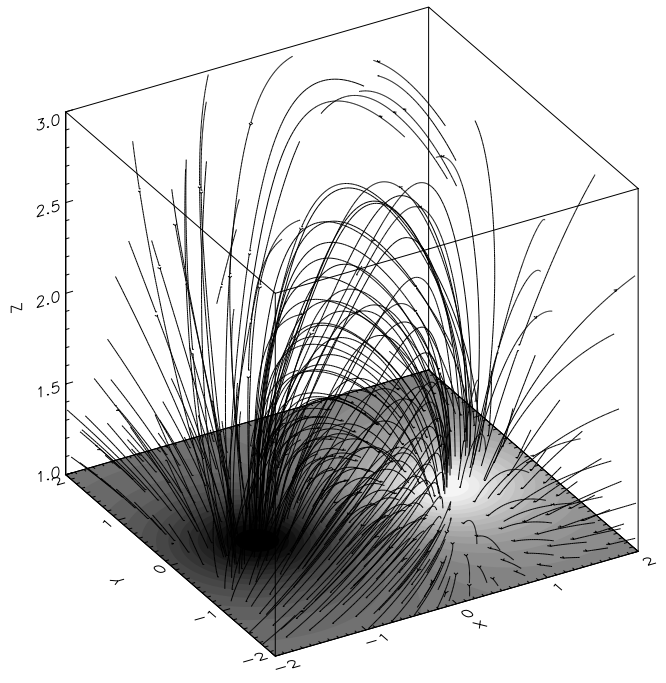

FIG. 4.—Three-dimensional structure of the current carrying force-free initial magnetic field ($\alpha = 0.5$) of the model active region. The sigmoid structure of the field lines is evident. The intensity plot at $z = 0$ of the B_z component shows the polarity of the field (dark is negative and bright is positive polarity). This figure is also available as an mpeg animation showing the impact of the wave in the electronic edition of the *Astrophysical Journal*.

the Sun's mass, m_p the proton mass, $R_\odot$ the solar radius, the height is in units of 0.1 $R_\odot$, and n_0 is the normalizing density. The values of the parameters are given in the next section.

4. NUMERICAL RESULTS

In order to study the three-dimensional evolution of the EIT waves, we model the impact of the waves on an active region by using the magnetic field model given by equations (5)–(10) and gravitationally stratified initial density given by equation (14). We solve the three-dimensional resistive MHD equations with finite thermal pressure and an isothermal energy equation using the Lax-Wendroff method with a fourth-order Chebychev smoothing term added for numerical stability (Hamming 1973, pp. 571–572). The Lax-Wendroff method was found to be efficient for this problem and easily optimized for parallel processing supercomputers. The resolution in the present study was 128^3 grid points. An earlier version of this code was used successfully to study the three-dimensional nonlinear evolution and dissipation of Alfvén waves in coronal loops (see Ofman & Davila 1996, and references within).

The normalization parameters were the density $n_0 = 10^9$ cm^{-3}, the magnetic field $B_0 = 85$ G, the temperature $T_0 = 10^6$ K, and the corresponding isothermal sound speed $c_s = 128.5$ km s^{-1}. The distances were scaled by 0.1 $R_\odot$, and the lower active region boundary was placed at $z = 1$. The velocities were normalized by an Alfvén speed $V_{A,0} = B_0/\left(4\pi n_0 m_p\right)^{1/2} = 5853$ km s^{-1}. The time was normalized by the Alfvén time $\tau_A = 0.1 R_\odot / V_{A,0} = 11.9$ s. The normalized scale height was $H = 8.7 \times 10^{-3}$. The magnetic Reynolds number was set to $S = 10^4$. The plasma β, which is the ratio of the magnetic pressure to the gas pressure, is $\ll 1$ in the center of the model active region. At the center of the lower boundary of the $\alpha = 0$ model active region, $\beta = 0.002$, while at the top of the active region ($x = y = 0,\ z = 4$), the value is $\beta = 0.08$. When $\alpha = 0.5$, the value of β increases from 0.0016 at $z = 1$ to 0.011 at $z = 4$. Because of the bipolar structure of the active region magnetic field, the value of β varies slowly between the poles and increases away from the poles, to values of order unity, consistent with the values found by Gary (2001). The initial velocity pulse (13) leads to the formation of the fast magnetosonic wave in the computational domain. The phase speed of the fast magnetosonic wave is given by

$$V_f = \left(\tfrac{1}{2}\{V_A^2 + C_s^2 + [(V_A^2 + C_s^2)^2 - 4C_s^2 V_A^2 \cos^2\theta]^{1/2}\}\right)^{1/2}, \quad (15)$$

where θ is the angle between the magnetic field and the propagating wave and V_A is the local Alfvén speed.

In Figure 5 we show the magnetic field, velocity, density, and current squared in a cut through the x-y plane at $z = 2.49$ of the model active region at $t = 20.3$ with the initial three-dimensional magnetic field ($\alpha = 0$) shown in Figure 3. The arrows show the direction of the fields and flows in the x-y plane, and the gray scale shows the magnitude of the variables. The wave is propagating

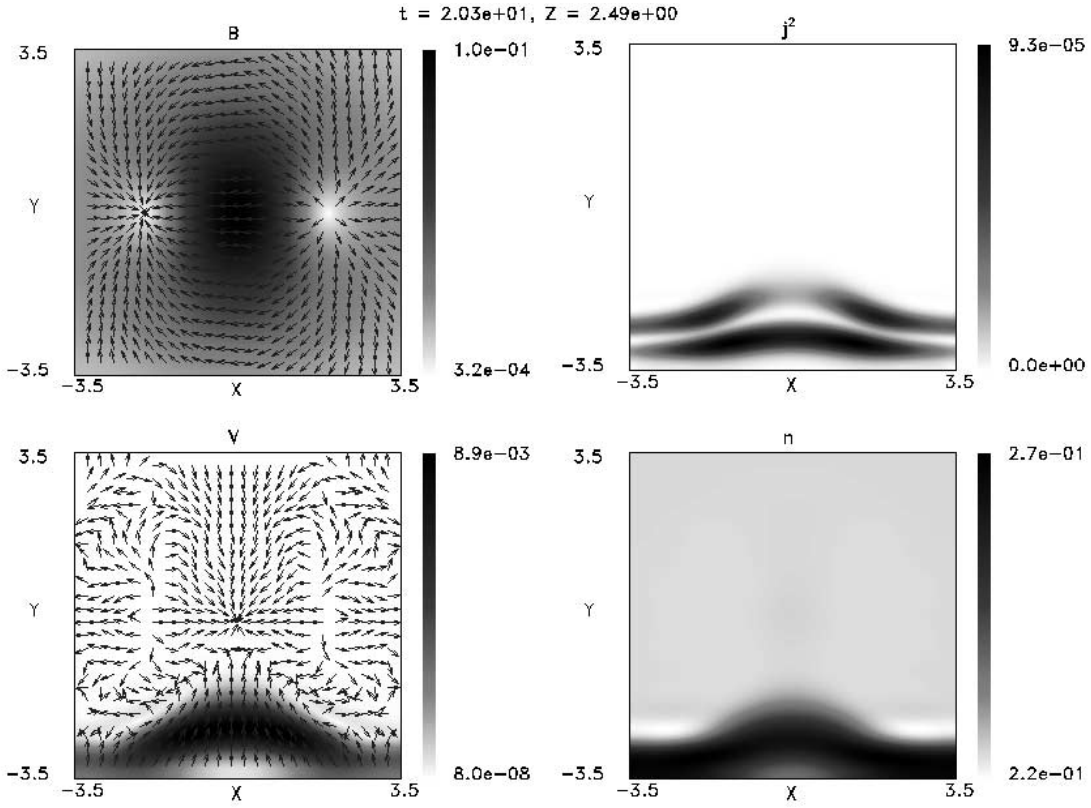

FIG. 5.—Magnetic field, velocity, density, and j^2 in the x-y plane at $z = 2.49$, and $t = 20.3$ of the incoming wave for the $\alpha = 0$ initial magnetic field. The arrows show the direction of the fields and flows, and the gray scale indicates the magnitude of the variables in this plane. The wave propagates from the x-z plane boundary into the active region. It is evident that the wave front is distorted by the nonuniform fast magnetosonic speed in the active region. The currents resulting from the distortion of the wave front resulting from the variation of the phase speed of the wave are evident. This figure is also available in color and as mpeg animations in the electronic edition of the *Astrophysical Journal.*

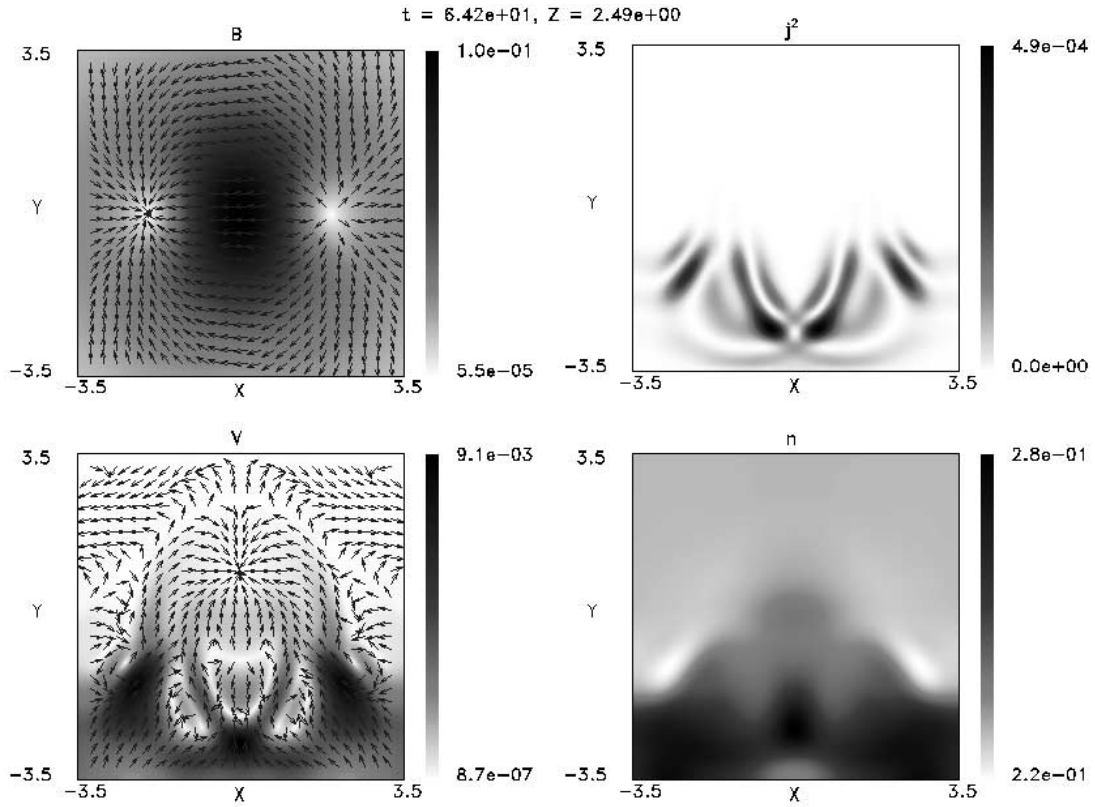

FIG. 6.—Magnetic field, velocity, density, and j^2 in the x-y plane at $z = 2.49$ and $t = 64.2$ of the scattered wave. The arrows show the direction of the fields and flows, and the gray scale indicates the magnitude of the variables in this plane. The wave propagates outward reflected by regions of high magnetic field in the active region. The currents resulting from the distortion of the wave front resulting from the variation of the phase speed of the wave and the magnetic field gradient are evident. This figure is also available in color in the electronic edition of the *Astrophysical Jorunal*.

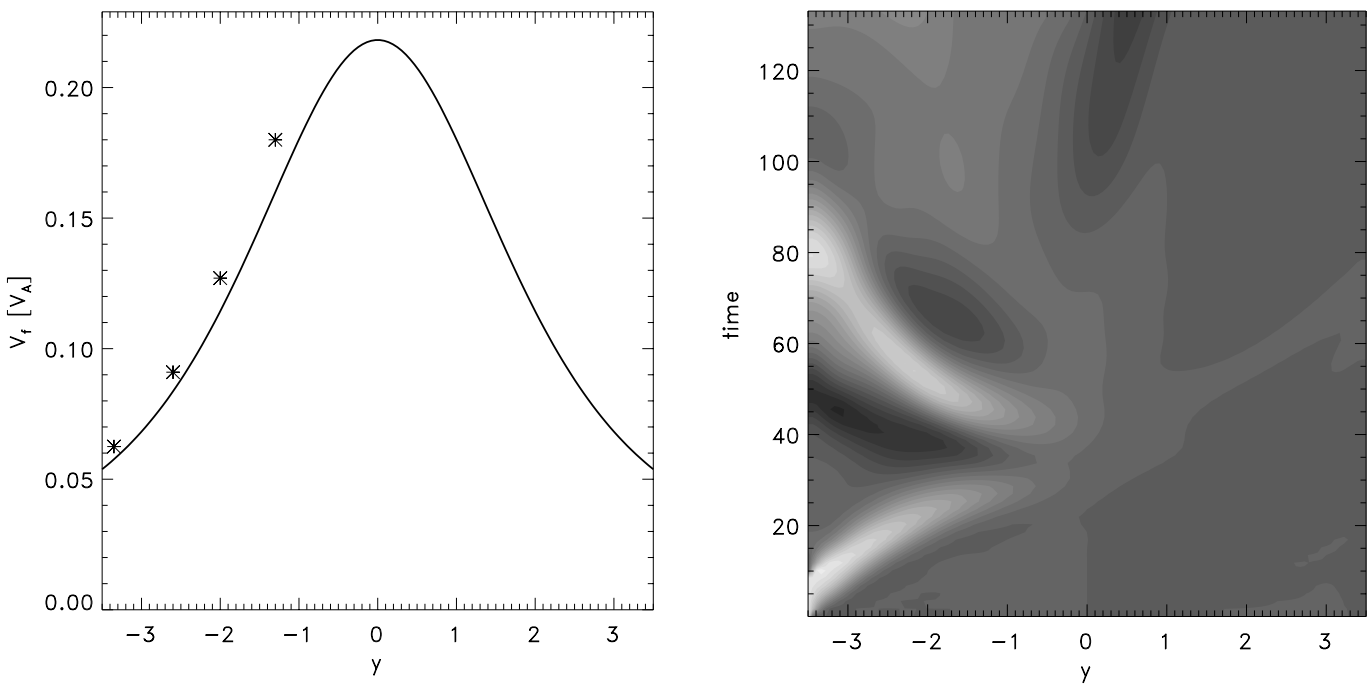

FIG. 7.—The left panel shows the y-dependence of the fast magnetosonic speed V_f near $x = 0, z = 2.49$ calculated using eq. (15) for the $\alpha = 0$ magnetic field. The right panel shows the propagation of the EIT wave along the y-direction at $z = 2.49$ and $x = 0$ in the simulation. The phase plot was obtained by plotting the amplitude of $V_y(y, t)$, with the brightest level corresponding to $V_y = 0.0125$ and the darkest level corresponding to $V_y = -0.0068$. The phase speed of the wave was computed from dy/dt along the trajectory and is shown with stars on the upper panel for several values of y. The incoming wave is evident at $0 < t < 35\tau_A$, and the reflected wave is evident at $t > 35\tau_A$. The transmitted wave is hardly seen at $y > 0$.

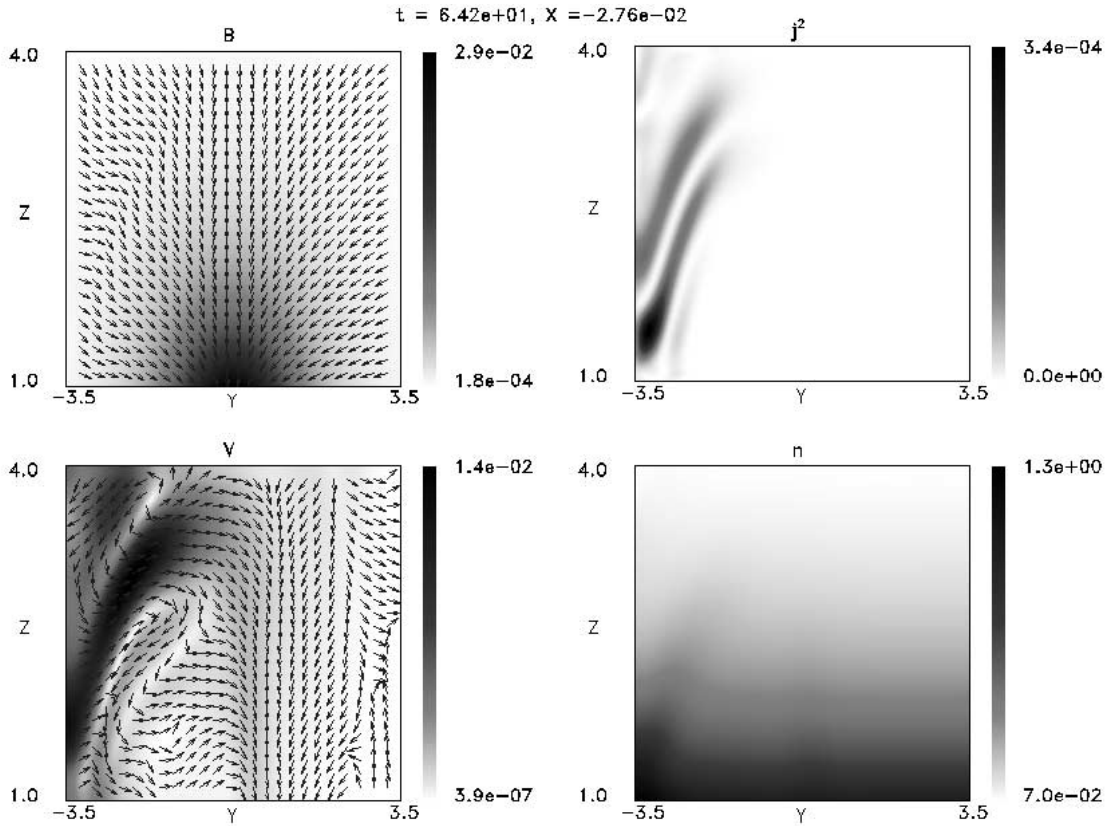

FIG. 8.—Magnetic field, velocity, density, and j^2 in the y-z plane at $x = -0.027$ and $t = 64.2$ of the scattered wave. The arrows show the direction of the fields and flows, and the gray scale indicates the magnitude of the variables in this plane. The current layers resulting from the outward-propagating wave are evident. The stratification of the density with height and the outward-propagating wave front of the reflected wave is seen. This figure is also available in color and as mpeg animations in the electronic edition of the *Astrophysical Journal.*

from the x-z plane boundary toward the positive y-direction. The density enhancement is associated with the velocity perturbation of the compressive fast magnetosonic wave. It is evident that the wave front is distorted by the nonuniform fast magnetosonic speed in the active region, with the central part propagating faster than the outlying regions as a result of the stronger magnetic field in this region (the sound speed is constant everywhere in

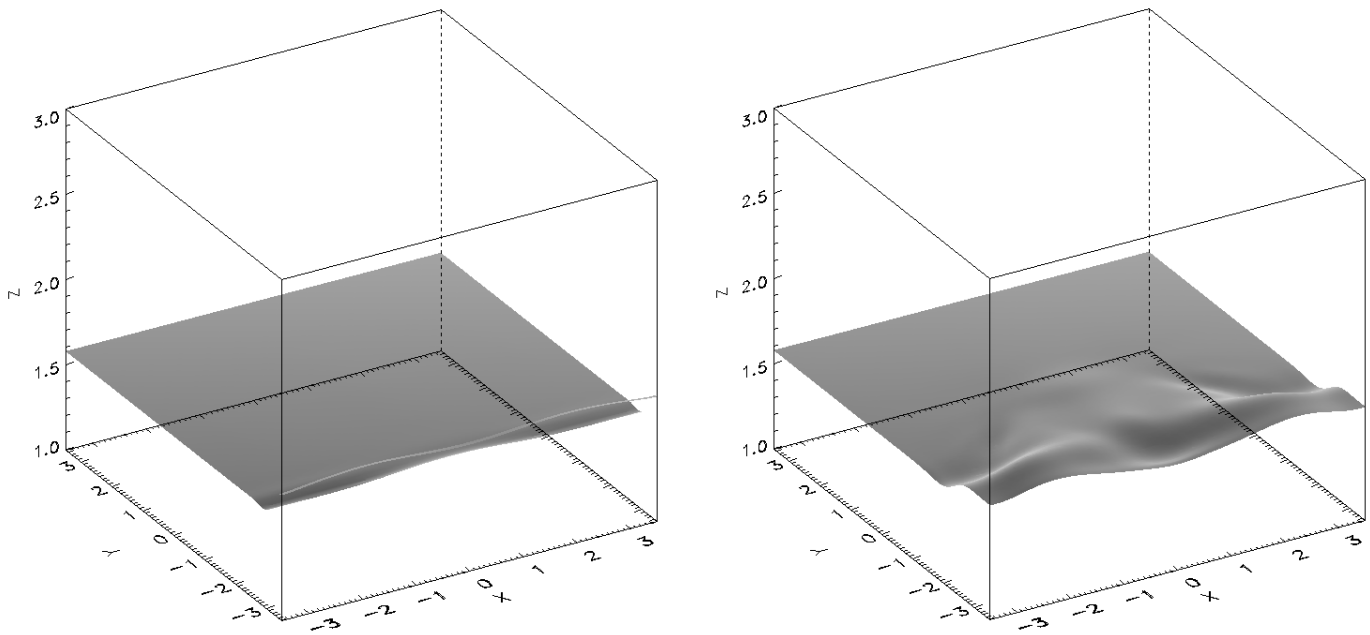

FIG. 9.—Three-dimensional isosurface plot of the density at the beginning of the run ($t = 20.3$, *left panel*) and at the end of the run ($t = 138.6$, *right panel*) for the $\alpha = 0$ case. The isosurface density level is $n = 0.4$.

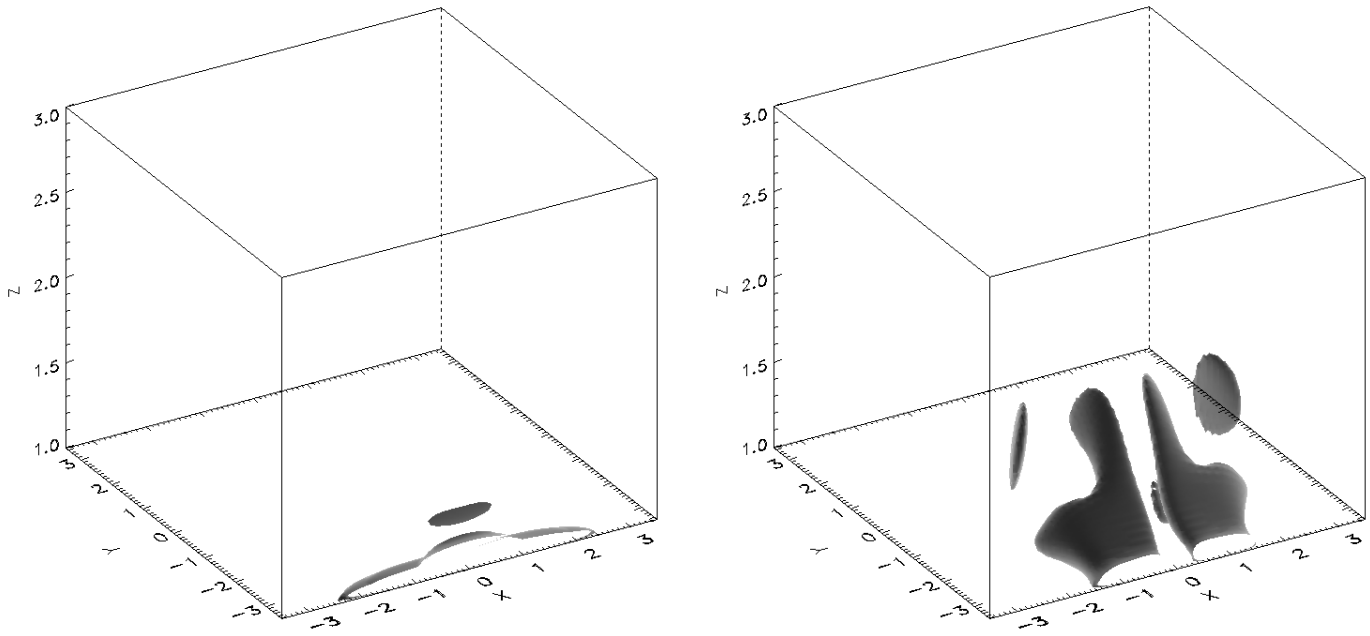

FIG. 10.—Three-dimensional isosurface plot of j^2 at the beginning ($t = 20.3$, *left panel*) and the end ($t = 138.6$, *right panel*) of the run for the $\alpha = 0$ case. The isosurface level is $j^2 = 2.4 \times 10^{-4}$.

this isothermal model). The currents resulting from the distortion of the wave front because of the variation of the phase speed and the gradients in the magnetic field are evident in the j^2 image.

The reflected wave generated as a result of the impact of the fast wave on the active region is shown in the x-y plane at a later time $t = 64.2$ in Figure 6. The wave propagates outward reflected at the footpoints and at regions of high fast magnetosonic wave speed, which corresponds to regions of strong magnetic field in the active region. The fine structure of the reflected waves is evident in the velocity components, density, and current associated with the wave. The outward wave follows the magnetic structure of the active region and consists of a reflected (toward the negative y-direction) and a small transmitted component. The transmitted component is negligible in the $y > 0$ region of the active region.

In the three-dimensional bipolar magnetic field and density structure, the propagation of the wave occurs in three dimensions and is not limited to a single plane. The figures at the x-y plane show only the parts of the three-dimensional wave that cross this plane. The waves are deflected by the curved field toward the footpoints of the magnetic loops. Since the boundary conditions require that the magnetic field is fixed at the lower boundary, the waves are reflected near the footpoints of the loops with small losses resulting from dissipation.

Because of the symmetry with respect to $x = 0$ of the $\alpha = 0$ magnetic field, it is possible to show the trajectory of the incident and the reflected wave in the y-t plane at $x = 0$ and fixed z. In Figure 7 we show the evolution of $V_y(y, t)$ near $x = 0$ and $z = 2.49$. The incoming wave is evident at $0 < t < 35\tau_A$, and the reflected wave is evident at $t > 35\tau_A$, with a small transmitted component at $y > 0$. The variation of the phase velocity of the wave is evident from the variation of dy/dt in this figure. From the top panel of Figure 7, we find that at the boundary the wave phase speed is about 320 km s^{-1}. The wave phase speed is about 1200 km s^{-1} near $y = 0$. We have estimated the values of dy/dt for several values of y (shown with stars on the upper panel) and found good agreement with the V_f given by equation (15).

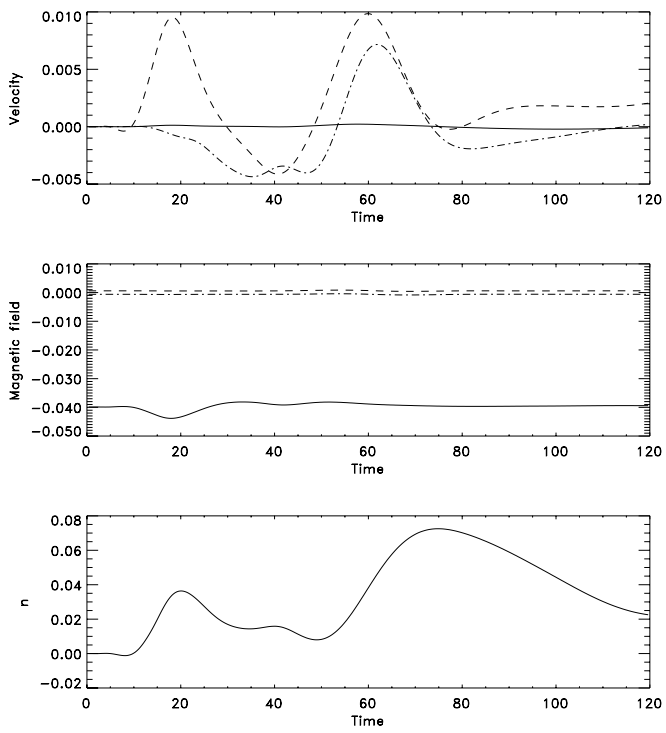

FIG. 11.—Temporal evolution of the velocity components (*upper panel*; V_x: *solid line*, V_y: *dashed line*, V_z: *dash-dotted line*) magnetic field components (*middle panel*; B_x: *solid line*, B_y: *dashed line*, B_z: *dash-dotted line*) and density (*lower panel*) at a point located at $x = -1.025$, $y = -2.5$, $z = 2.5$ in the $\alpha = 0$ model active region. The first peak in V_y at $t = 18.1$ and the corresponding variations in the other variables are due to the propagating wave, while the second peak in V_y at $t = 60.0$ is due to the reflected wave.

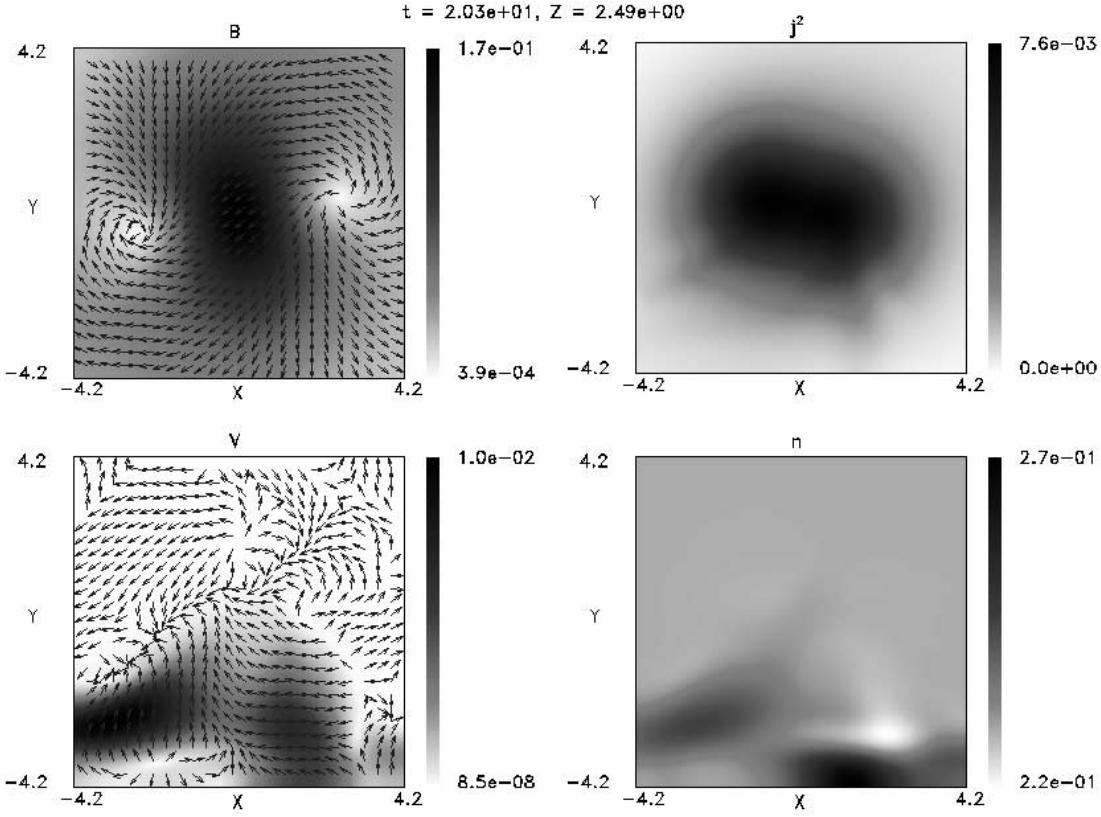

FIG. 12.—Magnetic field, velocity, density, and j^2 in the x-y plane at $z = 2.49$ and $t = 20.3$ of the incoming wave for the $\alpha = 0.5$ initial magnetic field. The arrows show the direction of the fields and flows, and the gray scale indicates the magnitude of the variables in this plane. The wave propagates from the x-z plane boundary into the active region. It is strongly distorted by the nonuniform and nonsymmetric magnetic field intensity in the active region. The background currents of the $\alpha = 0.5$ field with the currents resulting from the wave front are evident. This figure is also available in color and as mpeg animations in the electronic edition of the *Astrophysical Journal.*

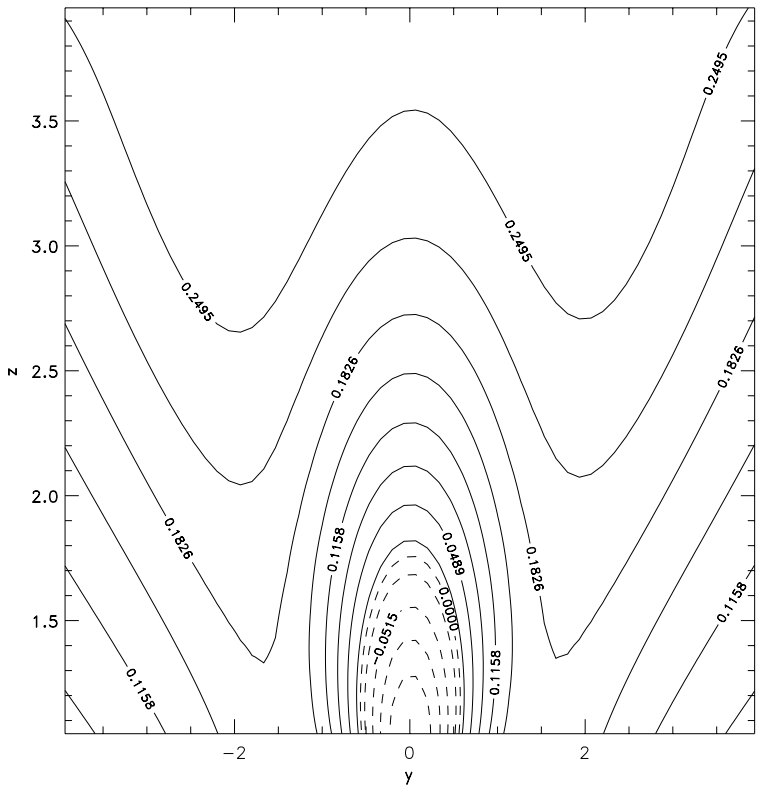

FIG. 13.—y-z dependence of $(d/dz)(B/\rho)$ of the $\alpha = 0.5$ active region at $x = 0$ and $t = 0$. The dashed contours indicate negative values of this quantity, indicating the area subject to the magnetic buoyancy instability (Priest 1984).

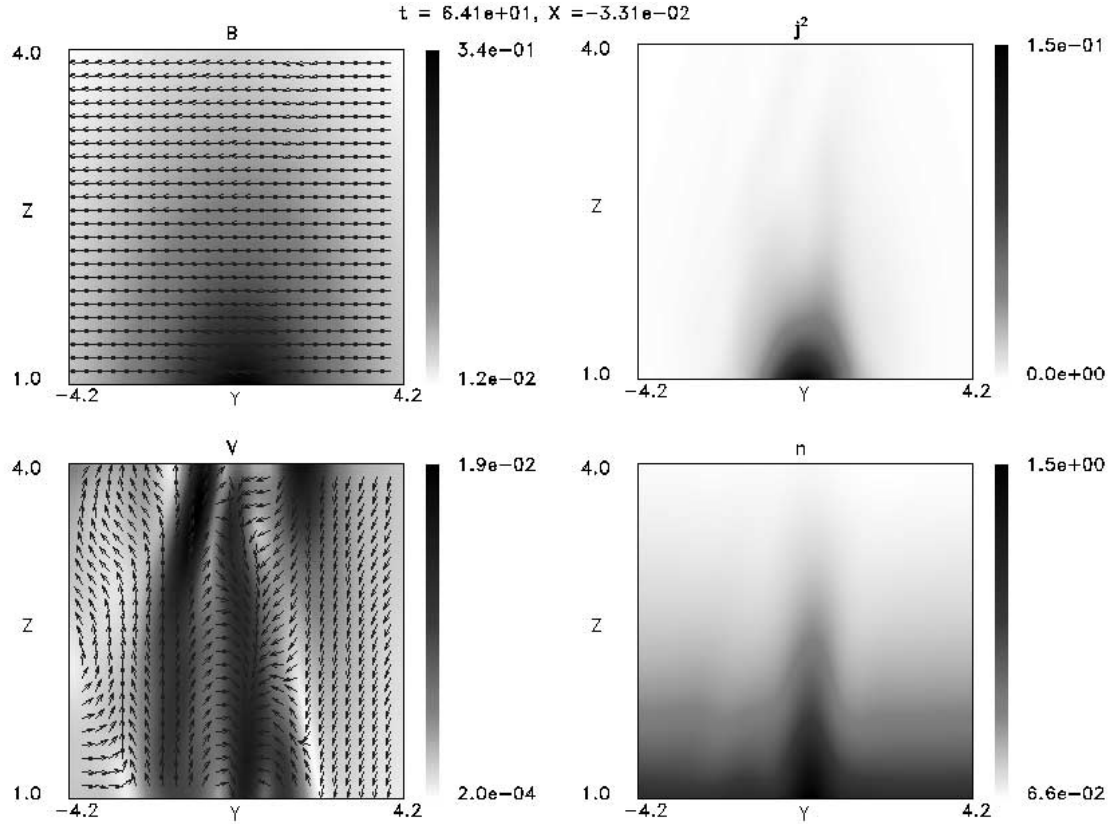

FIG. 14.—Magnetic field, velocity, density, and j^2 in the y-z plane at $x = -0.033$ and $t = 64.2$ of the incoming wave for the $\alpha = 0.5$ initial magnetic field. The arrows show the direction of the fields and flows, and the gray scale indicates the magnitude of the variables in this plane. The upflow and downflow of the active region material are evident. This figure is also available in color and as mpeg animations in the electronic edition of the *Astrophysical Journal.*

To show the structure of the reflected waves in the model active region with height, we present in Figure 8 the magnetic field, velocity, density, and j^2 in a cut through the y-z plane at $x = -0.0276$ and $t = 64.2$. The arrows indicate the direction of the fields and flows, and the gray scale indicates the magnitude of the variables in this plane. The seemingly abrupt change in the direction of the arrows in the left and upper parts of the magnetic field are due to the reflected

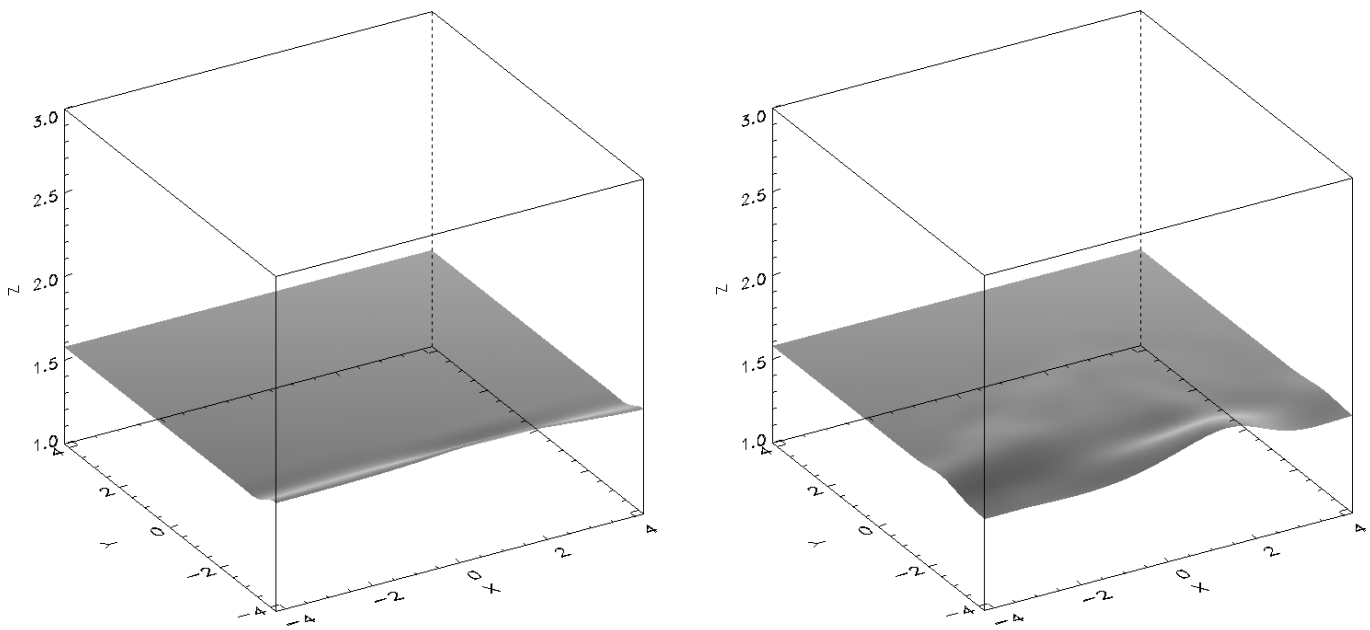

FIG. 15.—Three-dimensional isosurface plot of the density at the beginning of the run ($t = 20.3$, *left panel*) and at the end of the run ($t = 84.4$, *right panel*) for the $\alpha = 0.5$ case. The isosurface density level is $n = 0.4$.

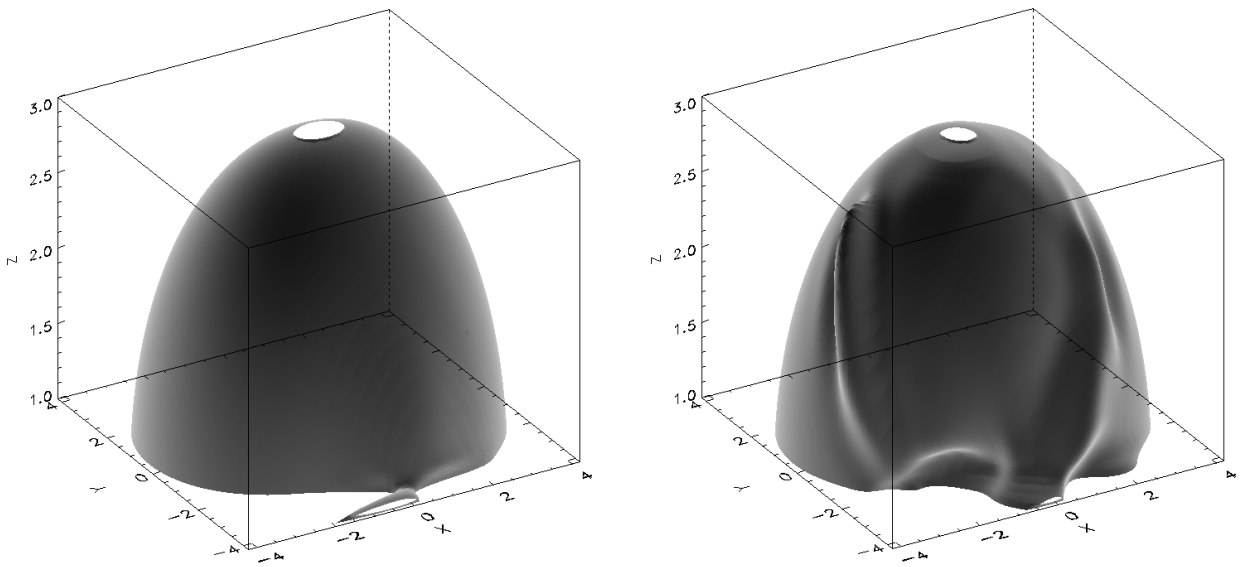

FIG. 16.—Three-dimensional isosurface plot of j^2 at the beginning of the run ($t = 20.3$, *left panel*) and at the end of the run ($t = 84.4$, *right panel*) for the $\alpha = 0.5$ case. The isosurface is $j^2 = 1.5 \times 10^{-3}$. The large-scale structure in j^2 is due to the background current of the active region magnetic field. The small-scale structures are due to the incident and the reflected fast magnetosonic waves.

wave fronts. The outward-propagating wave fronts of the reflected waves are apparent in the solutions and are most evident in the flow with vortices and in the current layers. The reflected waves are present in the left side of the active region (negative y-plane) since the magnetic field strength and V_f peak at the center of the region, and the footpoint reflection is directed toward the negative y-direction in this region. The three-dimensional magnetic field structure determines the structure of the wave fronts. The density is gravitationally stratified with small-scale perturbations induced by the waves.

In Figure 9 we show the isosurface plot of the density at the early stage of the run ($t = 20.3$, *upper panel*) and at the end of the run ($t = 138.6$, *lower panel*) for the $\alpha = 0$ case. The density is stratified on account of gravity with a small perturbation resulting from the incident and the reflected fast magnetosonic wave. The isosurface density level is $n = 0.4$, and the isosurface is nearly planar because of the gravitational stratification that dominates the density structure in z, and lack of significant density variations in x and y. The three-dimensional isosurface plot of j^2 at the same time at the beginning (*upper panel*) and the end (*lower panel*) of the run are shown in Figure 10. The perturbed current density resulting from the fast magnetosonic waves is evident. The isosurface level is $j^2 = 2.4 \times 10^{-4}$.

The temporal evolution of the velocity components, magnetic field components, and density at a point located at $x = -0.028$, $y = -2.5$, $z = 2.5$ in the model active region are shown in Figure 11. This point represents the oscillation of the magnetic field and plasma flow resulting from the impact of the EIT wave. The first peak in V_y at $t = 18.1$ and the corresponding variations in n and B_y are due to the propagating wave, while the second peak in V_y at $t = 60.0$ is due to the reflected wave. In addition, the reflected wave produces a peak in V_z at $t = 61.8$.

In Figure 12 we show the magnetic field, velocity, density, and j^2 in the x-y plane at $z = 2.49$ and $t = 20.3$ of the incoming wave for the current carrying $\alpha = 0.5$ initial magnetic field (Fig. 4). The arrows show the direction of the fields and flows, and the gray scale shows the magnitude of the variables in this plane. Note the sigmoid structure of the field reminiscent of the observed active regions most likely to erupt (e.g., Sterling et al. 2000). The wave propagates from

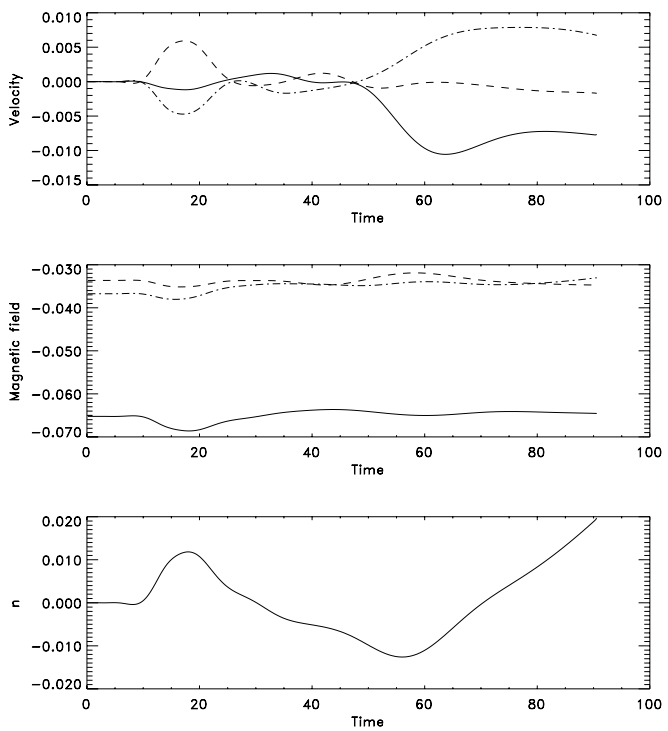

FIG. 17.—Temporal evolution of the velocity components (*upper panel*; V_x: *solid line*, V_y: *dashed line*, V_z: *dash-dotted line*) magnetic field components (*middle panel*; B_x: *solid line*, B_y: *dashed line*, B_z: *dash-dotted line*) and density (*lower panel*) at a point located at $x = -0.028$, $y = -2.5$, $z = 2.5$ in the $\alpha = 0.5$ model active region. The peak in V_y at $t = 17.3$ with the corresponding fluctuation in n and the other variables is due to the propagating wave. The reflected wave appears in V_y at $t = 41.6$. The fluctuations induced by the wave induce secondary flows and compression that destabilizes the region.

the x-z plane boundary into the active region. The currents of the $\alpha = 0.5$ field combined with the currents resulting from the impact of the wave front are evident. The currents are strong compared to the $\alpha = 0$ case, which contains only currents due to the wave. The asymmetry of the $\alpha = 0.5$ magnetic field with respect to $x = 0$ leads to strong distortion and interference of the wave front of the incoming wave, compared to the symmetric $\alpha = 0$ case in Figure 5.

According to linear analysis of planar field in stratified plasma, the development of the magnetic buoyancy instability is expected when the field strength falls off faster than the density in the active region, i.e., $(d/dz)(B/\rho) < 0$ (e.g., Priest 1984). The EIT wave is the perturbation that leads to the onset of the instability in the model active region. In Figure 13 we show the y-z dependence near $x = 0$ of $(d/dz)(B/\rho)$ for the $\alpha = 0.5$ active region at $t = 0$. The dashed contours indicate negative values of this quantity, indicating the area unstable to the magnetic buoyancy instability. The destabilization of the $\alpha = 0.5$ model active region becomes apparent at later times. In Figure 14 we show the magnetic field, velocity, density, and j^2 in the y-z plane at $x = -0.033$ and $t = 64.1$. Steady flows have formed through the upper boundaries. The jetlike flow of materials in the upward and downward directions in the active region is associated with the instability. Strong density compression has formed in the central part of the active region, in qualitative agreement with the area subject to the magnetic buoyancy instability shown in Figure 13. At later times the instability is evolving rapidly, and with the present resolution and time step we are not able to follow the instability numerically to much later times.

The three-dimensional isosurface plot of the density at the beginning of the run ($t = 20.3$, *upper panel*) and at the end of the run ($t = 84.4$, *lower panel*) for the $\alpha = 0.5$ case is shown in Figure 15. The isosurface density level is $n = 0.4$. The perturbations in the gravitationally stratified density caused by the waves are evident. The three-dimensional isosurface plot of j^2 at the beginning of the run (*upper panel*) and at the end of the run (*lower panel*) is shown in Figure 16. The isosurface is $j^2 = 1.5 \times 10^{-3}$. The large-scale structure in j^2 is due to the background current of the active region magnetic field. The small-scale structures are due to the incident and the reflected fast magnetosonic waves.

In Figure 17 we show the temporal evolution of the velocity components (*upper panel*) magnetic field components (*middle panel*) and density (*lower panel*) at a point located at $x = -1.025$, $y = -2.5$, $z = 2.5$ in the $\alpha = 0.5$ model active region. The peak in V_y at $t = 17.3$ with the corresponding fluctuation in n and the other variables is due to the propagating wave. The reflected wave appears in V_y at $t = 41.6$. However, at this location it is not evident in the other variables. The fluctuations induced by the wave induce secondary steady flows at $t > 50$ and compression that destabilizes the region.

5. DISCUSSION AND CONCLUSIONS

We present the first three-dimensional numerical model of the local interaction between fast magnetosonic waves and active regions using a resistive three-dimensional MHD model with gravity and finite plasma pressure. We show that many aspects of the simulation match observations of coronal waves impacting active regions. The loops in Figure 3 can be compared with the loops at the top of the *TRACE* image in Figure 2. The wave passage in the *TRACE* observations consisted of a deflection of the field lines to the north, followed by a return to their original positions. This deflection also appears in the simulation shown in Figures 5–12. Unfortunately, the *TRACE* observations ceased shortly after the wave was observed to impact the active region loops, so we were unable to detect any lingering oscillations or reflections to compare with the model results. Oscillations of individual loops caused by wave trapping were observed by Aschwanden et al. (1999) and Nakariakov et al. (1999). However, wave trapping in individual loops is not modeled in the present study since the density structure in the model lacks the fine structure seen in *TRACE*.

We have demonstrated that an incident MHD wave can have an impact on an active region, and the model results also show the strong impact the region has on the wave. The wave's trajectory is completely modified: we observe strong reflection, refraction, and dissipation of the wave with very little transmission. As in the EIT observations, the simulation shows very little evidence of the wave transmission through the active region, with most of the wave being reflected and refracted away from the active region toward regions of lower magnetic field as seen in Figure 6. Additionally, the model (as seen in Fig. 8) indicates that a significant fraction of the wave energy can be transported toward higher altitudes as a result of reflection at the footpoints. At higher altitude it is more difficult to observe the waves with EUV images because of the weak emission. At present, three-dimensional observations of active regions are not available. Three-dimensional observations of the corona may become possible in the future with the planned *STEREO* mission (Davila, Rust, & Sharer 2000).

We find that when the active region contains currents ($\alpha = 0.5$), the impact of the waves destabilizes the region and leads to strong upflows and downflows of the plasma, in addition to excitation of secondary waves. This numerical result is in qualitative agreement with observations and can explain the observed "sympathetic flaring" phenomena. The destabilization of the region could occur as a result of the magnetic buoyancy instability that grows when the field strength falls off faster then the density (e.g., Priest 1984). This instability could be triggered by the impact of the fast magnetosonic waves on a current-carrying active region.

Biesecker & Thompson (2000) found no increase in the rate of flaring following an EIT wave compared to the rate of flaring prior to a wave. However, a Monte Carlo simulation of the distribution of times between successive flares indicated that if the contribution of sympathetic flares was less than 20% of the total, the data used in the study would not be sufficient to detect the presence of sympathetic flaring. The model indicates that a magnetic region impacted by an EIT wave can be strongly influenced and possibly destabilized by the incident perturbation. The frequency at which this might occur may be below the threshold of observability for many correlation studies. However, it should be possible to observe specific cases that involve the oscillation of magnetic fields and flaring in response to an MHD wave. Should EUV and/or Hα observations of this type become available, we anticipate adapting the model in this paper to simulate evolution, periodicity, and dissipation derived from the data analysis.

L. O. would like to acknowledge support by the NASA SR&T and the NASA Sun Earth Connection Theory program. A major part of this work was done while L. O. was visiting at the Department of Geophysics, Tel Aviv University. We would like to thank M. Wills-Davey for providing some of the figures for this paper and V. M. Nakariakov for useful discussions.

REFERENCES

Aschwanden, M. J., Fletcher, L., Schrijver, C. J., & Alexander, D. 1999, ApJ, 520, 880
Becker, U. 1958, Z. Astrophys., 44, 243
Biesecker, D. A., & Thompson, B. J. 2000, J. Atmos. Sol.-Terr. Phys., 62, 1449
Cuperman, S., Ofman, L., & Semel, M. 1989, A&A, 216, 265
Davila, J. M., Rust, D. M., Sharer, P. J. 2000, AAS/Solar Physics Division Meeting, 32, 0293
Gary, G. A. 2001, Sol. Phys., 203, 71
Hamming, R. W. 1973, Numerical Methods for Scientists and Engineers (2d ed.; New York: McGraw-Hill)
Handy, B. N., Bruner, M. E., Tarbell, T. D., Title, A. M., Wolfson, C. J., Laforge, M. J., & Oliver, J. J. 1998, Sol. Phys., 183, 29
Khan, J. I., & Hudson, H. S. 2000, Geophys. Res. Lett., 27, 1083
Klassen, A., Aurass, H., Klein, K.-L., Hofmann, A., & Mann, G. 1999, A&A, 343, 287
Krucker, S., Larson, D. E., Lin, R. P., & Thompson, B. J. 1999, ApJ, 519, 864
Moreton, G. F. 1961, S&T, 21, 145
Murawski, K., Nakariakov, V. M., & Pelinovsky, E. N. 2001, A&A, 366, 306
Nakariakov, V. M., & Ofman, L. 2001, A&A, 372, L53
Nakariakov, V. M., Ofman, L., DeLuca, E., Roberts, B., Davila, J. M. 1999, Science, 285, 862
Norton, H. R. 2001, AGU, Spring Meeting 2001, abstract SH41B-12
Ofman, L., & Davila, J. M. 1996, ApJ, 456, L123
Pinter, S., & Dryer, M. 1977, Akad. Nauk SSSR Izv. Ser. Fiz., 41, 1849
Priest, E. R. 1984, Solar Magnetohydrodynamics (Geophys. & Astrophys. Monogr.; Dordrecht: Reidel), 1984
Ramsey, H. E., & Smith, S. F. 1966, AJ, 71, 197
Richardson, R. S. 1951, ApJ, 114, 356
Roberts, B., Edwin, P. M., Benz, A. O. 1983, Nature, 305, 688
———. 1984, ApJ, 279, 857
Sakai, J. I., Kawata, T., Yoshida, K., Furusawa, K., & Cramer, N. F. 2000, ApJ, 537, 1063
Smith, S. F., & Harvey, K. L. 1971, Physics of the Solar Corona, ed. C. J. Macris (Astrophys. & Space Sci. Library 27; Dordrecht: Reidel), 156
Schnack, D. D., & Killeen 1980, J. Comp. Phys., 35, 110
Sterling, A. C., Hudson, H. S., Thompson, B. J., & Zarro, D. M. 2000, ApJ, 532, 628
Thompson, B. J., et al. 1999, ApJ, 517, L151
———. 2000, Sol. Phys., 193, 161
Valniček, B. 1964, Bull. Astron. Inst. Czechoslovakia, 15, 207
Wang, H., Chae, J., Yurchyshyn, V., Yang, G., Steinegger, M., & Goode, P. 2001, ApJ, 559, 1171
Wang, Y.-M. 2000, ApJ, 543, L89
Warmuth, A., Vršnak, B., Aurass, H., & Hanslmeier, A. 2001, ApJ, 560, L105
Wills-Davey, M. J., & Thompson, B. J. 1999, Sol. Phys., 190, 467
Wu, S. T., et al. 2001, J. Geophys. Res., 106, 25,089